Chapter 4

Effects of Voids in Tensile Single-Crystal Cu Nanobeams

Aylin Ahadi, Per Hansson and Solveig Melin

Additional information is available at the end of the chapter

http://dx.doi.org/10.5772/intechopen.74169

Abstract

Molecular dynamic simulations of defect nanosized beams of single-crystal Cu, loaded in displacement controlled tension until rupture, have been performed. The defects are square-shaped, through-the-thickness voids of different sizes, placed centrally in the beams. Three different cross section sizes and two different crystallographic orientations are investigated. As expected, the sizes of the beam cross section and the void as well as the crystal orientation strongly influence both the elastic and the plastic behaviors of the beams. It was seen that the strain at plastic initiation increases with beam cross section size as well as with decreasing void size. It is further observed that the void deformed in different ways depending on cross section and void size. Sometimes void closure, leading to necking of the beam cross section followed by rupture occurred. In other cases, the void elongated leading to that the two ligaments above and below the void ruptured independently.

Keywords: molecular dynamics, nanobeams, single-crystal Cu, voided tensile beams

1. Introduction

Nanotechnology provides applications in an increasing number of engineering fields, with tailor manufactured products for everyday use. Mobile phones, medical sensors and solar cells are examples of well-established application areas. However, since it is an experimentally verified fact that nanosized structures respond differently on mechanical loading than macroscopic structures of the same material, design and dimensioning of nanocomponents lack a solid ground corresponding to traditional dimensioning handbook rules at the macroscale.

The reason for traditional engineering dimensioning rules becoming obsolete at small enough metric scales is that, with decreasing structural size, the number of surface close atoms as compared to number of bulk atoms increases and, at some point, no longer is negligible. Electron redistribution close to the surfaces will leave the surface close atoms in energy states deviating from those of bulk atoms. This influences the interatomic bonding forces and, thereby, the material response to mechanical loading as discussed by e.g., [1–3]. This effect is accentuated if the atoms are placed at, or close to, corners and edges of the structure, e.g., [4]. As a consequence, the material properties will vary with size for small enough structures, and the effects become obvious below about 50–100 nm.

Also, the crystallographic orientation is of uttermost importance for the material properties, e.g., [5, 6]. The crystallographic orientation imposes anisotropy in the structure and also decides the surface topology which influences the mechanical properties. The orientation further sets the preferred slip plane directions and, thereby, influences the plasticity development.

Here, the tensile response of single-crystal nanosized Cu beams, holding square-shaped, through-the-thickness voids, will be investigated with respect to elastic and plastic behavior and eventual size dependence in the mechanical response. The rational for this investigation is that even if defect-free structures might be intended at manufacturing, defects will always be present to some extent. If their presence influences the mechanical response of the structure, the product functionality might be at risk.

To this end, 3D single-crystal nanosized Cu beams of different cross section sizes, holding through-the-thickness voids of different sizes, will be investigated using the molecular dynamics free-ware large-scale atomic/molecular massively parallel simulator (LAMMPS), see [7]. The loading will be displacement controlled tension along the length direction, and two different crystallographic orientations will be considered and compared.

2. Geometry and boundary conditions

The structures considered are single-crystal face centered cubic (fcc) Cu beams of length $L = 100a_0$ and square cross section with three different side lengths $s = 6Na_0$, $N = 1, 2, 3$, with $a_0 = 3.615$ Å denoting the lattice parameter for Cu. Each beam holds a symmetrically placed, square-shaped through-the-thickness void of width w and height h, cf. **Figure 1(a)** where a centrally placed coordinate system (x, y, z) is introduced. The sensitivity to voids will be investigated by varying the width w, keeping the relative void height $h = s/3$ constant.

Two different crystallographic orientations are considered to determine its influence on the mechanical response. For the first orientation, referred to as the [100]-orientation, the coordinates (x, y, z) coincide with crystallographic directions according to: x = [100], y = [010] and z = [001], cf. **Figure 1(b)**. For the second, referred to as the [110]-orientation, x = [110], y = [−110] and z = [001], cf. **Figure 1(c)**.

A beam is built from the repetition of fcc Cu unit cells, and to mimic clamped end boundary conditions, all atoms within four unit cells at each end of the beam are restricted from movements in the y- and z-directions. During the relaxation step, one atom is fixed in all directions.

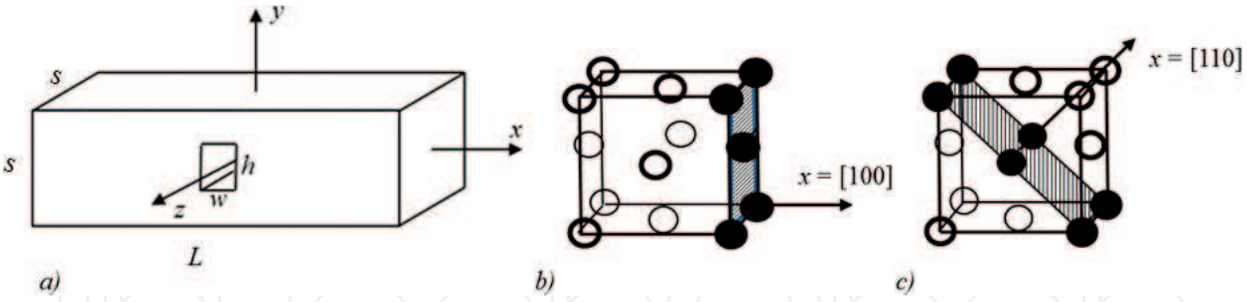

Figure 1. (a) Beam configuration and coordinate system. (b) and (c) Crystallographic orientations.

The atoms in between the clamped ends are free to move in all directions without constraints. The beams are loaded in tension along the x-axis until final rupture. The load is displacement controlled through applying a constant velocity, $v_{end,}$ in the $+x$- and $-x$-directions to all atoms within the clamped beam ends.

3. Molecular dynamic simulations

3.1. Simulation procedure

For the simulations, the molecular dynamics free-ware LAMMPS has been employed and the atomic images are produced using OVITO, developed by [8].

In the simulations, an NVT-ensemble, with constant number of particles N, constant volume V and absolute temperature T, kept at a constant temperature of 0.01 K through a Nosé-Hoover thermostat as found in [9] is employed. Before load application, relaxation of the atomic ensemble in order to reach the equilibrium state is imposed during 5000 time steps, with each time step equal to 5 fs. This gives the relaxation time equal to 25 ps, which was found to be sufficiently long to reach equilibrium with good accuracy as judged from the variations in axial stress with time. Thereafter, a constant velocity of $v_{end} = a_0/200/\text{ps}$ is imposed in the $+x$- and $-x$-directions at all atoms within the clamped ends using a constant time step of 5 fs.

3.2. Interatomic potential

To calculate the atomic interactions, an embedded atom method (EAM) potential according to [10, 11] is employed. The potential has one pair-wise repulsive and one N-body attractive part and the potential energy E_i of atom i is given by:

$$E_i = f\left(\sum_{j \neq i} \rho(r^{ij})\right) + \frac{1}{2}\sum_{j \neq i} \phi(r^{ij}) \tag{1}$$

where r^{ij} is the distance between atoms i and j, ϕ is a pair-wise potential function, ρ is the contribution to the electron charge density from atom j at the location of atom i and f is an embedding function that represents the energy required to place atom i into the electron cloud. For the present study, the potential file Cu_u3.eam, provided by LAMMPS and developed by [12], is used.

3.3. Centrosymmetry parameter

The results are evaluated and illustrated using the centrosymmetry parameter, *CSP*, as defined by [13]. The *CSP* is a measure of the deviation from a perfect lattice configuration, and for an atom, the *CSP* is defined according to

$$CSP = \sum_{i=1}^{N/2} \left| \mathbf{R}_i + \mathbf{R}_{i+N/2} \right|^2 \tag{2}$$

Here, N is the number of nearest neighbors in the lattice surrounding the atom, equal to 12 for an fcc lattice. The vectors $\mathbf{R}_i$ and $\mathbf{R}_{i+N/2}$ are the vector pairs of opposite nearest-neighbors to the atom. For a perfect lattice, the *CSP*, through the definition (Eq. (2)), becomes $CSP < 3$. Since the *CSP* of an atom is a measure of the positions of the atoms nearest neighbor pairs, both crystallographic orientation and structure geometry are of importance. For the present crystallographic orientations and beam geometries, *CSP* values for atoms located at surfaces, edges and corners are shown in **Table 1**. In the present investigation, the *CSP* reached values up to 60 for atoms situated at or close to corners and edges. Values in the interval between 9 and 21 are found for atoms affected by local defects such as voids, partial dislocations or stacking faults.

As an illustration of the placements of atoms with $CSP > 21$, a beam with orientation [100] is shown at two different strain levels in **Figure 2**. In the figure, each individual atom is shown as a filled circle, with color according to the *CSP* value. In **Figure 2**, all atoms with $CSP \leq 21$ are colored red; the rest, found at edges and at corners, have their *CSP* in the interval $21 < CSP \leq 60$. **Figure 2(a)** shows the situation directly after relaxation, at zero axial load, with high *CSP* values along the edges of the beam, and **Figure 2(b)** at an axial strain of $\varepsilon_x = 0.1$, where also edges that have emerged through slip events attain high *CSP* values.

Lattice structure	*CSP*
Ideal fcc structure	$CSP < 3$
Fault sites	$3 \leq CSP < 9$
Surface atoms [100]	$9 \leq CSP < 21$
Surface atoms [110]	$9 \leq CSP < 25$
Edge and corner atoms [100]	$CSP \geq 21$
Edge and corner atoms [110]	$CSP \geq 25$

Table 1. *CSP* values for present geometries and orientations.

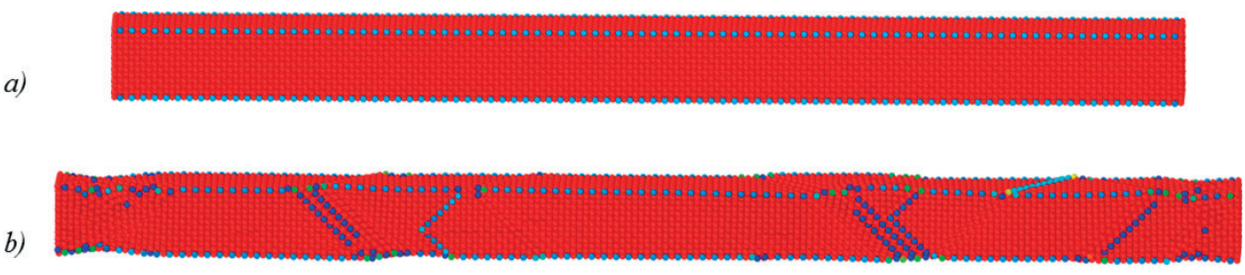

Figure 2. Red atoms: $CSP \leq 21$, nonred atoms: $21 < CSP \leq 60$. [100]-orientation and $s = 6a_0$. (a) $\varepsilon x = 0$ and (b) $\varepsilon x = 0.1$.

4. Results and discussion

4.1. Recorded strain levels

Beams of geometry according to **Figure 1**, holding voids with aspect ratios w/h = 1, 2, 3, 4, are loaded under displacement controlled tension until final rupture. After an initially elastic phase, plasticity will appear through slip along close-packed {111} planes. For each case, the strain at plastic initiation, ε_i, the strain ε_{mc} at eventual closure of the mid-section of the void, the strain at eventual total void closure, ε_c and the strain at rupture were determined through monitoring the instantaneous *CSP* values for all atoms during the loading process. If the beam ruptures due to necking as a result of void closure, this strain is denoted ε_{f1}. In case the void does not close, but instead expands so that the ligaments above and below the void rupture independently, these strains are denoted ε_{f1} and ε_{f2}. Recorded strains are plotted for each beam size and orientation in **Figure 3**, and the values are given in **Table 2**.

4.2. Elastic response

In **Figure 4**, all strains at plastic initiation, taken from **Table 2**, have been merged for comparison; in **Figure 4(a)**, for the [100] orientation and in **Figure 4(b)**, for the [110] orientation. From simulations of solid beams, it was observed that the strain at plastic initiation, ε_i, is, in practice, independent on cross section size for each orientation as also concluded in e.g., [14], where pure metric scaling effects were investigated for solid single-crystal Cu beams. In [14], it was found that $\varepsilon_i \approx 0.094$ for the [100] orientation and $\varepsilon_i \approx 0.068$ for the [110] orientation, so that the [110] orientation yields first, with the ratio between initiation strains about 0.7. The values for solid beams are included in **Figure 4** as circles at $w/h = 0$. As seen in **Figure 4**, ε_i tends to increase with beam cross section size as well as with decreasing ratio w/h for both orientations. It can also be noted that ε_i for the solid beams is markedly higher than for the voided beams, and in all cases, the [110] orientation initiates first.

The higher initiation strain for solid beams is expected since a void acts as a local stress raiser, weakening the structure.

Another observation is that the initiation strain for the two thicker beams, with $s = 12a_0$ and $s = 18a_0$, is relatively close in comparison with the thinnest with $s = 6a_0$, which initiates at markedly lower strains for both orientations. This indicates that a limiting value is approached with increasing s. A comparison of the initiation strains between solid beams, ε_{isolid}, and beams holding the smallest voids with $w/h = 1$ shows that, for both orientations, $\varepsilon_i/\varepsilon_{isolid} \approx 0.3$ for $s = 6a_0$ and $\varepsilon_i/\varepsilon_{isolid} \approx 0.6$ for $s = 12a_0$ and $s = 18a_0$ so that the void influence has decreased. Even so, the influence from a void, even if small, is always present.

4.3. Atomic arrangements during plastic deformation for the [100] orientation

Starting with the [100] orientation, with recorded strains in **Table 2** and plotted in **Figure 3(a)**, **(c)** and **(e)**, it is seen that for the smallest cross section, $s = 6a_0$ **Figure 3(a)**, the void closes in all cases except for $w/h = 1$. For the other ratios of w/h, still for $s = 6a_0$, the voids close first at the middle of the void at strain ε_{cm}, thus forming two separate voids. Final void closure appears shortly after, at ε_c, where after rupture occurs at ε_{f1}. The different scenarios are shown in **Figure 5**.

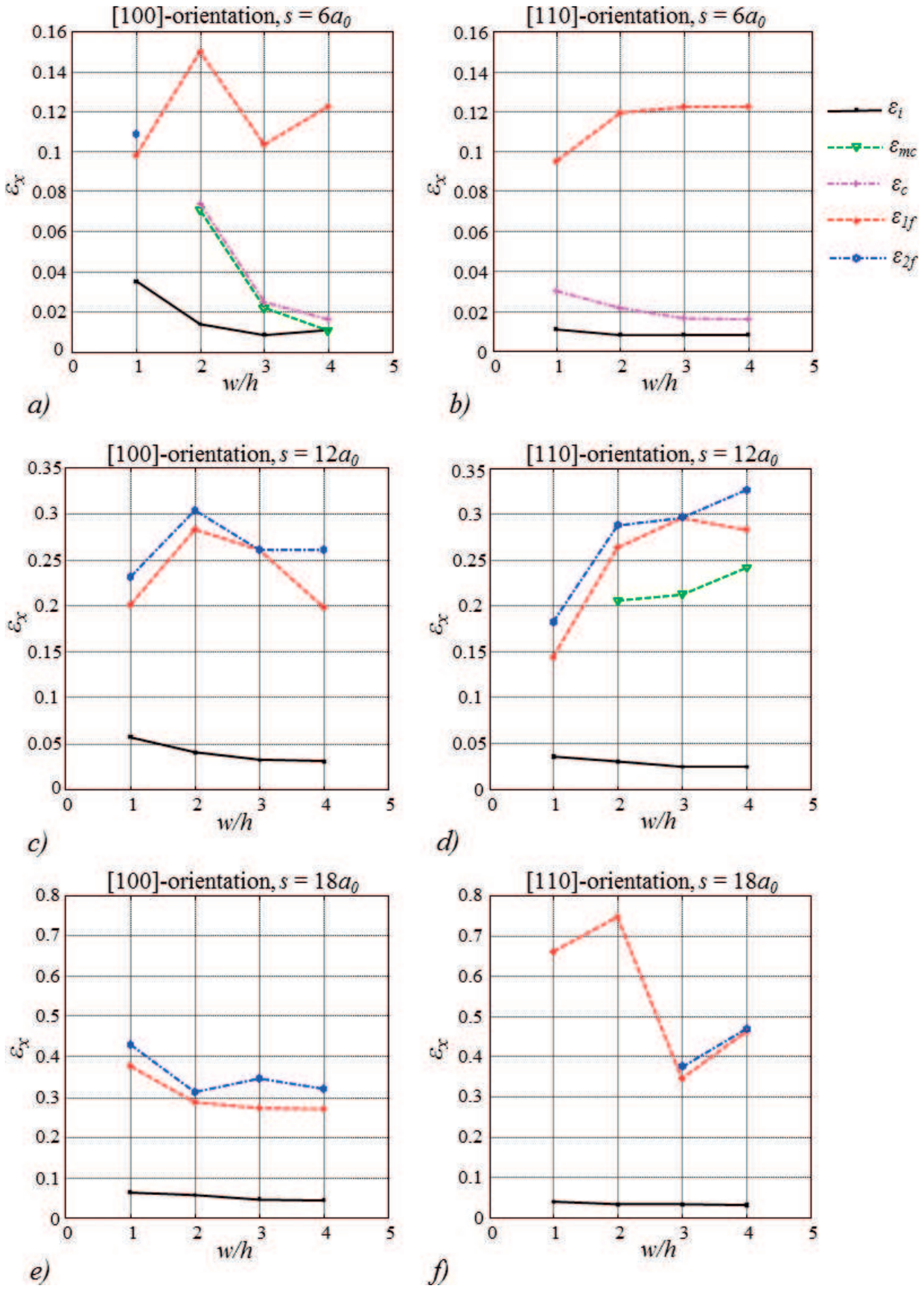

Figure 3. Strains at plastic initiation, ε_i, at closure of the mid-section of the void, ε_{mc}, at void closure ε_c and at ruptures ε_{f1} and ε_{f2}. (a), (c) and (e): [100] orientation. (b), (d) and (f): [110] orientation. Values from **Table 2**.

***w/h*, [100] $s = 6a_0$**	ε_i	ε_{cm}	ε_c	ε_{f1}	ε_{f2}
1	0.0353	—	—	0.0978	0.1087
2	0.0136	0.0707	0.0734	0.1495	—
3	0.0082	0.0217	0.0245	0.1033	—
4	0.0108	0.0109	0.0162	0.1223	—
w/h, [110] $s = 6a_0$					
1	0.0109	—	0.0299	0.0951	—
2	0.0082	—	0.0217	0.1196	—
3	0.0082	—	0.0163	0.1223	—
4	0.0082	—	0.0162	0.1223	—
w/h, [100] $s = 12a_0$					
1	0.0571	—	—	0.2011	0.2310
2	0.0408	—	—	0.2826	0.3043
3	0.0326	—	—	0.2609	0.2609
4	0.0300	—	—	0.1984	0.2609
w/h, [110] $s = 12a_0$					
1	0.0353	—	—	0.1440	0.1821
2	0.0299	0.2065	—	0.2636	0.2880
3	0.0245	0.2120	—	0.2962	0.2962
4	0.0245	0.2418	—	0.2826	0.3261
w/h, [100] $s = 18a_0$					
1	0.0625	—	—	0.3777	0.4293
2	0.0571	—	—	0.2853	0.3125
3	0.0462	—	—	0.2717	0.3451
4	0.0435	—	—	0.2690	0.3206
w/h, [110] $s = 18a_0$					
1	0.0380	—	—	0.6603	—
2	0.0326	—	—	0.7470	—
3	0.0326	—	—	0.3451	0.3750
4	0.0299	—	—	0.4620	0.4701

Table 2. Strains at plastic initiation, ε_i, at closure of the mid-section of the void, ε_{mc}, at void closure ε_c and at ruptures ε_{f1} and ε_{f2}. Graphs in **Figure 3**.

In the case $s = 6a_0$ and $w/h = 1$, the void expands and the two ligaments above and below the void rupture independently at ε_{f1} and ε_{f2}. Snapshots of the events during deformation for this case are shown in **Figure 5(a)–(c)**, coded in the *CSP*. The state $\varepsilon_x = 0$ is taken directly after relaxation. Activated {111} slip planes are seen to appear after plastic initiation and spread along the entire beam.

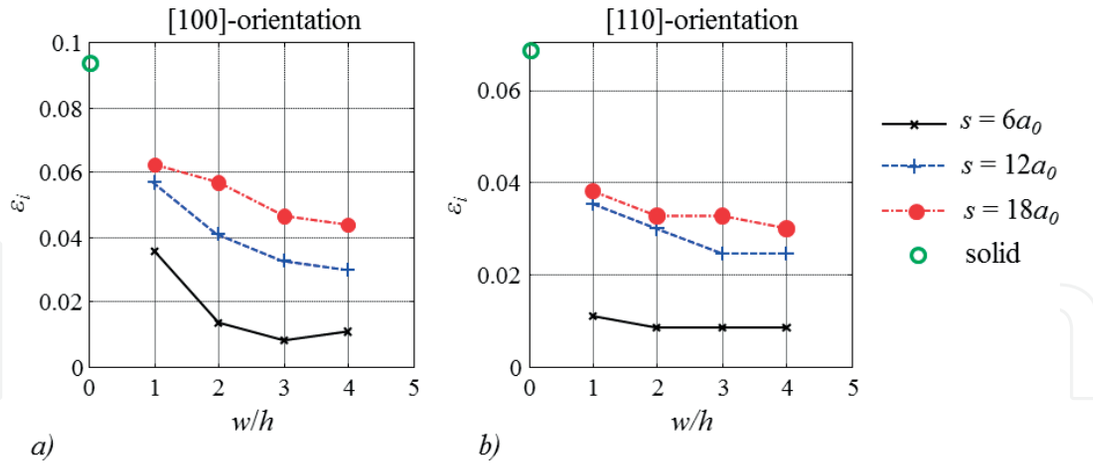

Figure 4. Strains at plastic initiation ε_i. (a) [100] orientation and (b) [110] orientation.

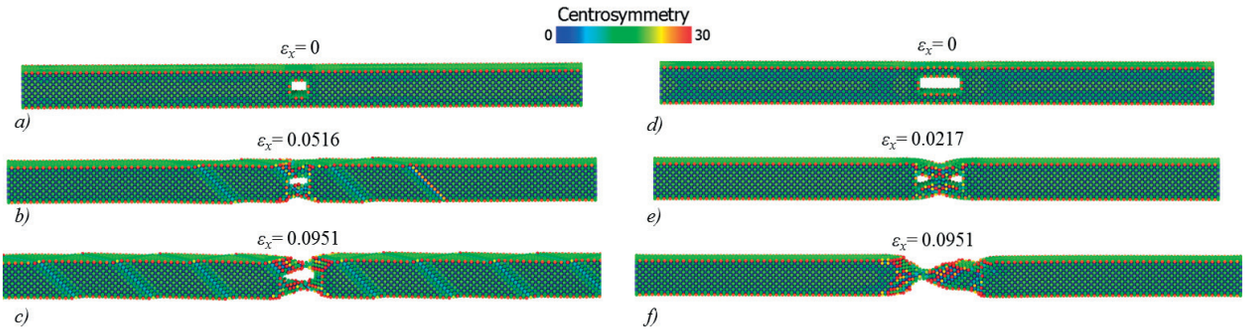

Figure 5. Events during deformation of beams with $s = 6a_0$ and (a)–(c) $w/h = 1$ and (d)–(f) $w/h = 3$. [100] orientation. Coded in the *CSP*. The states $\varepsilon_x = 0$ are taken directly after relaxation.

An example of a sequence of events during void closure is seen in **Figure 5(d)–(f)** for $s = 6a_0$ and $w/h = 3$. As seen, the void closes first at the center of the void, forming two separate voids which both close shortly after formation. This leads to that the initially voided but now healed cross-sectional part necks, and final rupture occurs at the strain ε_{f1}, cf. **Figure 3(a)**. Also, here the {111} slip planes are activated, but localization of the plasticity to the formerly voided region, followed by rupture, occurs before the plasticity has reached the beam ends. Instead, elastic regions remain away from the necking region.

For the larger beam cross sections, $s = 12a_0$ and $s = 18a_0$, no void closure occurs. Instead, the voids expand and the ligaments above and below the void rupture independently at ε_{f1} and ε_{f2}. The series of events are thus similar to what is seen in **Figure 5(a)–(c)**.

4.4. Atomic arrangements during plastic deformation for the [110] orientation

For the [110] orientation and $s = 6a_0$, **Figure 3(b)**, total closure of the voids occurs for all w/h where after the now solid center cross section ruptures at strain ε_{f1}. The voids are filled, atom plane by atom plane, from one side of the void to the other like a zipper, through slip along {111} planes. The case $s = 6a_0$, $w/h = 1$ is illustrated in **Figure 5(a)–(c)**, where the configuration

directly after relaxation, at $\varepsilon_x = 0$, is included. As seen, the plasticity in this case is localized to the void vicinity, similar to the case of void closure for the [100] orientation and $s = 6a_0$ in **Figure 5(d)–(f)**.

A comparison between the corresponding relaxed states for the [100]- and the [110] orientations, at $\varepsilon_x = 0$, shows the impact of crystallographic orientation. The [110] orientation creates a more roughened surface as compared to the [100] orientation. Comparing **Figures 5(a)** and **6(a)**, with the thinnest ligaments surrounding the voids and thus the weakest cross sections, it is seen that the deformation of the void in the relaxed state is much more obvious for the [110] orientation. The void seems to bulge due to the lower constraints on the atoms in combination with the orientations of the preferred {111} slip planes for the [110] orientation.

Increasing the cross section size to $s = 12a_0$, **Figure 3(d)**, displays a different deformation pattern. In all cases, the void is expanding, so that two ligaments rupture individually above and below the growing void at strains ε_{f1} and ε_{f2}. But for all cases apart from $w/h = 1$, the initial voids first close at the center, thus forming two separate voids. One of these will grow until the ligaments above and below it rupture at strains ε_{f1} and ε_{f2}. This is illustrated in **Figure 6(d)–(f)** for $w/h = 2$.

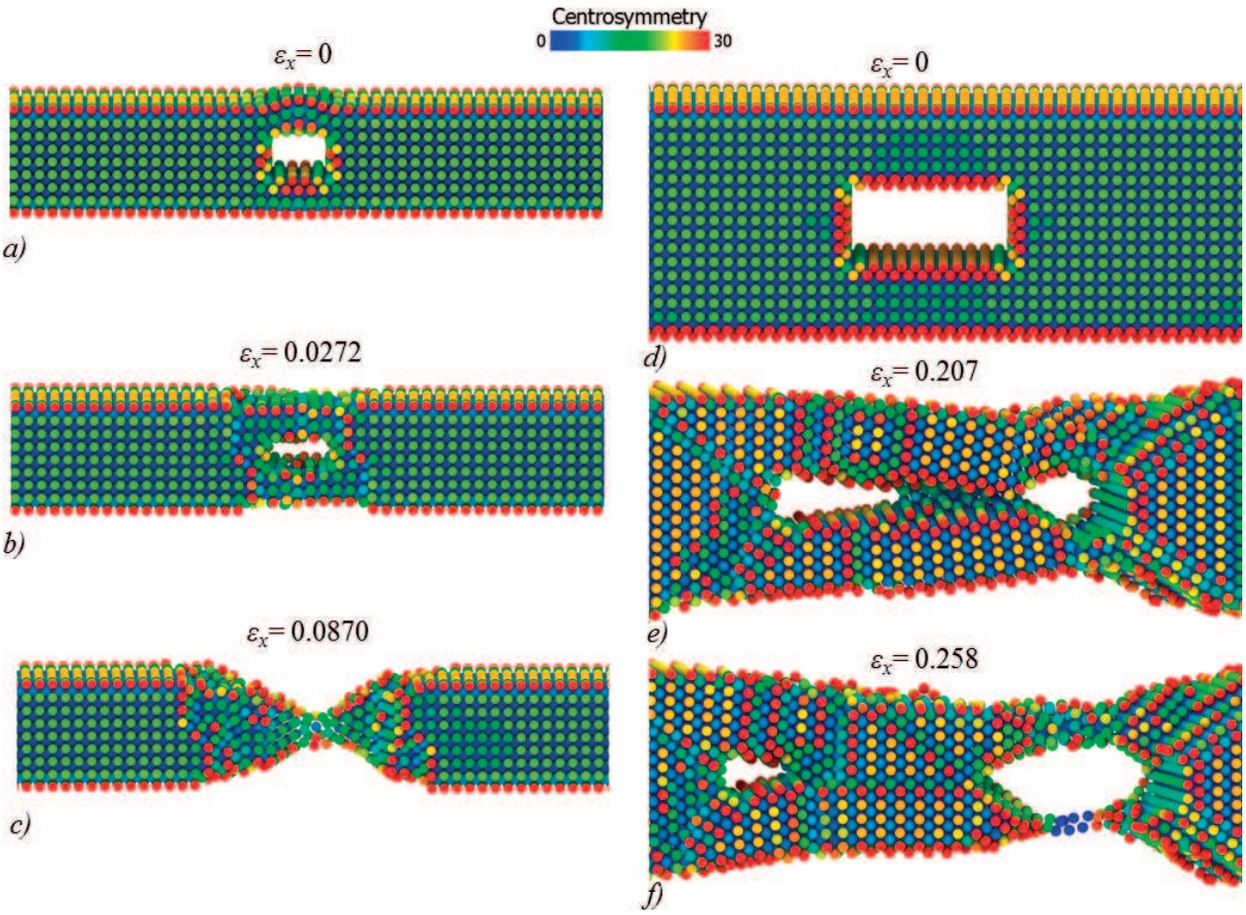

Figure 6. Events during deformation of beams with (a)–(c): $s = 6a_0$, $w/h = 1$, and (d)–(f): $s = 12a_0$, $w/h = 2$. [110] orientation. Coded in the *CSP*. The states $\varepsilon_x = 0$ are taken directly after relaxation.

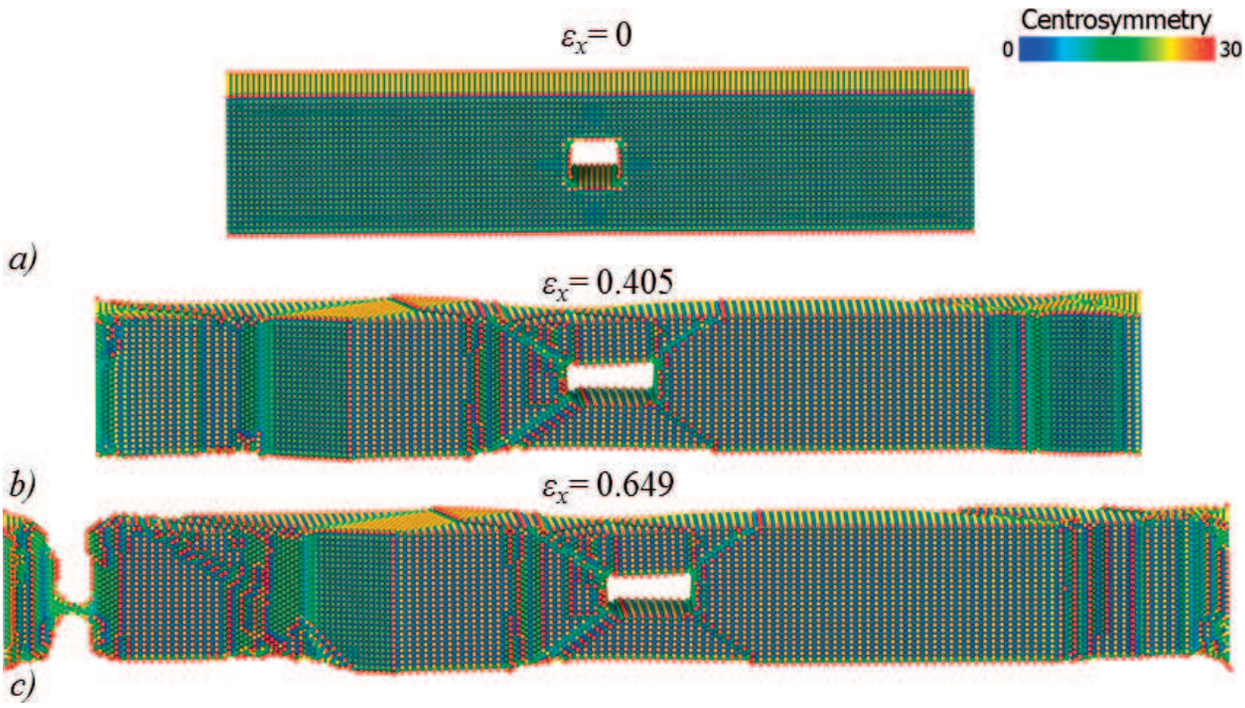

Figure 7. Events during deformation of beams with s = 18a$_0$ and w/h = 1. [110] orientation. Coded in the *CSP*. At (a) ε_x = 0, taken directly after relaxation, (b) ε_x = 0.405 and (c) ε_x = 0.649.

For $s = 18a_0$ in the [110] orientation with curves in **Figure 3(f)**, lastly, another phenomenon appears for $w/h = 1$ and $w/h = 2$. For these cases, initiation of plasticity as well as rupture occurs away from the void as illustrated in **Figure 7** for $s = 18a_0$ and $w/h = 1$. For the larger w/h, $w/h = 3$ and $w/h = 4$, the voids elongate and the ligaments rupture individually over the void similar to the events in **Figure 5(a)–(c)**.

5. Summary

Molecular dynamic simulations of beams of single-crystal Cu of dimensions $100a_0 \times s \times s$, $s = 6Na_0$, $N = 1, 2, 3$, and with a_0 denoting the lattice parameter of Cu, have been loaded in displacement controlled tension until rupture. Each beam holds a centrally placed, rectangular through-the-thickness defect of extension along the beam length direction equal to w and of height $h = s/3$. Aspect ratios $w/h = 1, 2, 3, 4$ were considered and the loading was applied along two crystallographic directions, the [100]- or the [110] direction, cf. **Figure 1**. The deformation development was monitored continuously and the strains at plastic initiation, at void closure and at rupture were recorded. The result is given in **Table 2** and visualized in **Figure 3**.

By studying **Figure 3** and **Table 2**, some general trends about the deformation behavior can be drawn. First in the case of total closure of the beams for $s = 6a_0$ for both crystallographic orientations, it is observed that the closure strain ε_c steadily decreases as the void width w increases. It is also observed that the strain at rupture is in the same range for both orientations for different values of s and, for both orientations, the values increase dramatically in magnitude with increasing s. Finally, it can be observed that no general trend regarding the

influence of w/h on the failure strain can be drawn. In some cases, the strain increases, and in some cases, it decreases with increasing value of w/h.

It was concluded that geometrical features such as beam size and crystallographic orientation played a crucial role for the mechanical behavior. Plasticity develops through slip along closed packed {111} planes, and the [110] orientation always initiates plasticity first. Further, the strain at plastic initiation increases with beam cross section size as well as with decreasing ratio w/h for both orientations.

Studying the deformation pattern, it was found that the plasticity developed and the void deformed in different ways depending on cross section size, void aspect ratio and crystal orientation. As regards the events that lead to final rupture of the beams, different scenarios were observed.

In some cases, the void elongated and the two beam ligaments, above and below the void, eventually necked and ruptured independently. In such cases, the plasticity, through slip along {111} planes before the last ligament rupture, tended to extend away from the regions near the void and could sometimes reach the beam ends.

In the cases where closure of the voids occurred, the strain at closure decreased with increasing w/h. Also, it was observed that the strain at failure was relatively independent of crystallographic orientation and that it increased with increasing cross section size.

Sometimes the void first closes at the center, forming two separate voids. Then, two scenarios are possible. One is that the two voids both eventually close, followed by necking and rupture of the now healed cross section. In these cases, the plasticity localizes to the vicinity of the neck and leaves regions away from the neck elastic. The other possible scenario is that one of the created voids start to elongate and the ligaments above and below this void neck and rupture independently.

There were also cases where failure did not occur in the vicinity of the void; instead rupture occurred near one beam end after that the plasticity had spread over the entire beam.

Author details

Aylin Ahadi*, Per Hansson and Solveig Melin

*Address all correspondence to: aylin.ahadi@mek.lth.se

Division of Mechanics, LTH, Lund University, Lund, Sweden

References

[1] Hommel M, Kraft O. Deformation behavior of thin cupper films on deformable substrates. Acta Materialia. 2001;**49**:3935-3947. DOI: 10.1016/S1359-6454(01)00293-2

[2] Schweiger R, Dehm G, Kraft O. Cyclic deformation of polychrystalline Cu films. Philosophical Magazine. 2003;**83**:693-710. DOI: 10.1080/0141861021000056690

[3] Schweiger R, Kraft O. Size effects in the fatigue behavior in thin Ag films. Acta Materialia. 2003;**51**:195-206. DOI: 10.1016/S1359-6454(02)00391-9

[4] Melin S, Hansson P, Ahadi A. Defect sensitivity of single-crystal nano-sized Cu beams. Procedia Structural Integrity. 2016;**2**:1351-1358. DOI: 10.1016/j.prostr.2016.06.172

[5] Olsson PAT, Melin S. Atomistic studies of the elastic properties of metallic BCC nanowires and films. In: Pyrz R, Rauhe JC, editors. IUTAM Symposium on Modelling Nanomaterials and Nanosystems. Dordrecht, Netherlands: Springer Science+Buissness Media B.V; 2008

[6] Olsson PAT, Melin S, Persson C. Atomistic simulations of tensile and bending properties of single-crystal bcc iron nanobeams. Physical Review B. 2007;**76**:224112. DOI: 10.1103/PhysRevB.76.224112

[7] Sandia National Laboratories. LAMMPS. Available from: http://lammps.sandia.gov

[8] Stukowski A. Visualization and analysis of atomistic simulation data with OVITO—The open visualization tool. Modelling and Simulation in Materials Science and Engineering. 2010;**18**:015012. DOI: 10.1088/0965-0393/18/1/015012

[9] Ellad BT and Miller RE. Modeling Materials Continuum, Atomistic and Multiscale Techniques. Cambridge University Press; 2011. ISBN: 978052856980

[10] Holian BL, Ravelo R. Fracture simulations using large-scale molecular-dynamics. Physical Review B. 1995;**51**(17):11275-11288. DOI: 10.1103/PhysRevB.51.11275

[11] Holian BL, Voter AF, Wagner NJ, Ravelo RJ, Chen SP, Hoover WG, Hoover CG, Hammerberg JE, Dontjie TD. Effects of pair-wise versus many-body forces on high-stress plastic deformation. Physical Review A. 1991;**43**:2655-2661

[12] Foiles SM, Baskes MI, Daw MS. Embedded-atom-method functions for the fcc metals Cu, Ag, Au, Ni, Pd, Pt, and their alloys. Physical Review B. 1986;**33**(12):7983-7991. DOI: 10.1103/PhysRevB.33.7983

[13] Kelchner CL, Plimpton SJ, Hamilton JC. Dislocation nucleation and defect structure during surface indentation. Physical Review B. 1998;**58**:11085-11088. DOI: 10.1103/PhysRevB.58.11085

[14] Ahadi A, Hansson P, Melin S. Tensile behaviour of single-crystal nano-sized Cu beams—Geometric scaling effects. Computational Materials Science. 2017;**137**:127-133